

PCCP

Accepted Manuscript



This is an *Accepted Manuscript*, which has been through the Royal Society of Chemistry peer review process and has been accepted for publication.

Accepted Manuscripts are published online shortly after acceptance, before technical editing, formatting and proof reading. Using this free service, authors can make their results available to the community, in citable form, before we publish the edited article. We will replace this *Accepted Manuscript* with the edited and formatted *Advance Article* as soon as it is available.

You can find more information about *Accepted Manuscripts* in the [Information for Authors](#).

Please note that technical editing may introduce minor changes to the text and/or graphics, which may alter content. The journal's standard [Terms & Conditions](#) and the [Ethical guidelines](#) still apply. In no event shall the Royal Society of Chemistry be held responsible for any errors or omissions in this *Accepted Manuscript* or any consequences arising from the use of any information it contains.

Gold-Palladium core@shell nanoalloys: experiments and simulations

A. Spitale¹, M. A. Perez², S. Mejía-Rosales³, M. J. Yacamán⁴, M. M. Mariscal^{1*}

¹INFIQC, CONICET. Departamento de Matemática y Física, Facultad de Ciencias Químicas, Universidad Nacional de Córdoba. Córdoba. Argentina. X5000HUA.

²INFIQC, CONICET. Departamento de Fisicoquímica, Facultad de Ciencias Químicas, Universidad Nacional de Córdoba. Córdoba. Argentina. X5000HUA.

³Center for Innovation and Research in Engineering and Technology, and CICFIM-Facultad de Ciencias Físico-Matemáticas, Universidad Autónoma de Nuevo León, San Nicolás de los Garza, NL 66450, México.

⁴Department of Physics and Astronomy, University of Texas at San Antonio, One UTSA Circle, San Antonio, TX 78249

*E-mail: marcelo.mariscal@conicet.gov.ar

Abstract

In this work, we report a facile synthesis route, structural characterization, and full atomistic simulations of gold-palladium nanoalloys. Through aberration corrected-STEM, UV-vis and EDS chemical analysis, we were able to determine that Au(core)-Pd(shell) bimetallic nanoparticles were formed. Using different computational approaches, we were capable to establish how the size of the core and the thickness of the shell will affect the thermodynamic stability of several core-shell nanoalloys. Finally, grand canonical simulations using different sampling procedures were used to study the growth mechanism of Pd atoms on Au seeds of different shape.

Keywords: Au-Pd nanoparticles, core-shell, nanoalloys, grand canonical Langevin dynamics, STEM, EDS.

1. Introduction

It is very well known nowadays that metal clusters and nanoparticles (NPs) present exceptional optical, electrical and catalytic properties^{1,2}. The case of nanoalloys is of topmost interest and constitutes an innovative type of catalysts, mainly due to the fact that their physicochemical properties can be tuned by varying the composition and atomic arrangement as well as their sizes and shapes³. Among various nanoalloys, the system Pd-Au is one of the most attractive systems in catalysis⁴; since alloyed and core@shell Au-Pd structures have been used as catalysts in the oxidation reaction of CO at low temperatures⁵, acetylene to ethylene conversion⁶, oxidation of alcohols to aldehydes and production of vinyl acetate monomers, selective hydrogenation of butadiene⁷, the Ullmann reaction of aryl chlorides in water⁸, among others^{9,10,11}. Due to the widespread diversity of applications of Au-Pd nanocatalysts, it is crucial to comprehend the structure, surface composition and growth mechanism of AuPd nanoalloys.

In the past decade, several groups were able to determine that the synthesis conditions are crucial to obtain nanoalloys of various sizes, chemical composition and morphological structure. Interestingly, if the reduction reactions are conducted sequentially, then quite different results are obtained, which depend on the order in which the compounds are added. For instance, segregated structures have been reported, *i.e.* Pd(core)@Au(shell)¹², Au(core)@Pd(shell)^{13,14,15}, random solid solutions¹⁶, and multi-layer structures¹⁷. Li *et al.*¹⁸ produced Au@Pd nanoparticles by thermal decomposition of PdCl₂ on previously synthesized Au seeds, and Nutt *et al.*¹⁹ deposited Pd onto Au NPs. In both cases, it was found that the plasmon resonance of the Au rapidly disappeared. The observation of such a widespread variety of structures makes the study of this system even more attractive from a basic perspective.

From a theoretical perspective, the energetics, structures and segregation (chemical ordering) of Pd-Au nanoalloys have been reported, using genetic algorithms^{20,21} to find lowest-energy structures. In those works, the binding energy and the second difference in energy were used as stability criteria. Using different parameterizations of the Gupta potential, the authors found Pd(core)@Au(shell) segregation and Pd-Au mixing generally lead to mixed Pd-Au nanoalloys. Recently, Neyman *et al.*²² reported results from density

functional theory (DFT) calculations showing that segregation of Au atoms to the NP surface is thermodynamically favorable, where the most stable sites for Au substitution are located at the edges of the Pd-NPs. Moreover, the formation of structures with Au atoms located in the core of the nanoalloys was found to be energetically unfavorable with respect to monometallic Pd and Au NPs of the same shape and size. Oviedo *et al.*²³ show, by means of statistic thermodynamics framework, that while Au deposits on Pd cores may be thermodynamically more stable than the bulk Au material for certain NPs sizes, this is not the case for Pd deposits with respect to its bulk material.

In the present work, a combination of experimental and theoretical techniques is used to study the main growth sequences of the paradigmatic AuPd nanocatalysts. In particular, we report an experimental synthesis route to obtain Au@Pd core-shell nanoparticles of size less than 10nm. Imaging and chemical characterization were made using a multi-technique approach, i.e. with UV-spectroscopy, aberration corrected scanning transmission electron microscopy (Cs-STEM), and Energy Dispersive X-Ray spectroscopy (EDS). Subsequently, theoretical calculations, using embedded atom potentials were used to analyze the energetic stability of core-shell structures with different shell thickness, core sizes and shapes. Thereafter, full atomistic simulations under the grand canonical ensemble (μ, V, T) were employed to understand the growth mechanism of Pd atoms on Au seeds, in particular how the Pd atoms attach to the Au NP seed. Finally, the atomic configurations obtained by the grand canonical Monte Carlo (gcMC) and grand canonical Langevin Dynamics (gcLD) simulations were used as input to simulate HAADF-STEM images in order to compare experimental and simulation results.

2. Experimental Section

2.1 Chemicals and Materials

As precursor for the NPs, 0.25 mM tetrachloroauric(III) acid (HAuCl_4 , puriss p.a.) and 2.5 mM sodium tetrachloropalladate(II) (Na_2PdCl_4 , Sigma Aldrich $\geq 99.99\%$) stock solutions were prepared and protected from sunlight. Sodium borohydride (NaBH_4 , Tetrahedron) and hydroquinone (C_6H_4 -1,4-(OH)₂, Anedra) were used as reducing agents. Sulfuric acid (H_2SO_4 , Cicarelli 95-98%) and potassium bromide (KBr, Anedra) solutions

were prepared by dissolving the appropriate amount of the reagent in deionized water. All reagents were used as received.

2.2 Preparation of Au seeds and Au@Pd Bimetallic NPs

Gold nanoparticles were prepared by adding a freshly prepared solution of NaBH_4 (12 mM, 2 mL) to an ice cold (0 °C) aqueous solution of HAuCl_4 (3.9 mL, 0.254 mM), H_2SO_4 (1 mL, 1 mM) and water to reach a final volume of 10 mL, followed by vigorous mixing for 5 minutes. Before characterization by UV–vis spectroscopy, the stirring was stopped and the solution was left to warm for another 5 min until it reached room temperature. The nanoparticles were stored before being used to ensure that the maturation was completed.

Pd deposition onto the Au seeds was performed by using metastable Pd(II) solutions (baths), where the homogeneous nucleation of Pd NPs is inhibited. These baths generally contain 0.1 mM Na_2PdCl_4 , 0.1 mM HQ and 10 mM KBr. When gold seeds are added into these solutions, Pd(II) reduction is catalyzed and leads to palladium deposition at the surface of gold NPs, yielding Au@Pd NPs. 1 mL of Au seeds solution was diluted in 8 mL of water and 1 mL of Pd(II) bath was injected later. After 5 minutes of stirring, 100 μL of HQ 10 mM were added and the solution was left for 30 minutes with no agitation. Finally, two aliquots of 5 μL of Pd 10 mM were added 30 minutes apart. The samples for STEM analysis were taken at different stages of the reaction. This procedure is not usually employed, as in general the seeds are injected in the growth bath.

2.3 Characterization

UV-Visible spectra were recorded with a Shimadzu UV-1200 spectrometer, using a 1 cm quartz cell at room temperature to analyze the optical behavior of the samples.

Samples for characterization with Scanning Transmission Electron Microscopy (STEM, JEOL JEM-200ARMF, operating at 200 kV) were prepared without any purification treatment by seeding some drops of the colloidal solutions onto a grid covered with a holey carbon film. The grids were then washed in ethanol to remove any remaining molecules.

3. Model and Simulation Techniques

The standard ensemble to mimic crystal growth/dissolution is the grand canonical one, where the parameters fixed during the simulation are the volume of the simulation box (V), the temperature (T), and the chemical potential μ of the atoms being deposited (in this case, Pd). Thus, we have performed extensive grand canonical simulations using two different sampling algorithms (Metropolis Monte Carlo and Langevin Dynamics) to study the growth processes of AuPd nanoalloys.

The grand canonical - Langevin dynamics (gcLD) technique was originally developed by M. M. Mariscal and co-workers^{24,25} to study metallic deposition phenomena on crystalline planar surfaces (electrodes). Now, the method has been extended to non-planar systems, like clusters, nanowires and bimetallic nanoparticles (NPs). Langevin Dynamics is a method that extends molecular dynamics to represent the effect of perturbations caused by friction and eventual collisions occurring due to the presence of a solvent (the molecules in real systems hardly are under vacuum). For doing so, it makes use of stochastic differential equations, adding two terms to the Newton's second law to approximate the effects of neglected degrees of freedom. On the other hand, temperature can be controlled, approximating the canonical ensemble. Although it does not fully represent an implicit solvent (electrostatic screening and hydrophobicity), it mimics the viscosity of the medium.

The simulation cell contains two distinct regions: the NPs region, and a much larger solution region. Solvent is not modeled explicitly, but it is provided as a stochastic bath. Thus, the solution part contains only metal particles that can either be of the same element as the metal atoms of the nanoparticle or different from them. As stated above, all solution particles move according to Langevin's equation:

$$\frac{d\vec{v}}{dt} = -\frac{d\vec{r}}{dt}\gamma + \vec{F}_p + \vec{F}_r$$

where γ is the friction constant, \vec{F}_r represents the random force acting on each particle and \vec{F}_p represents the force due to the potential interaction (EAM) between the

particles and the NP, as they do not interact with each other. The friction constant γ and the random force \vec{F}_r are related by the fluctuation–dissipation theorem. The Langevin dynamics was implemented according to the Ermak's algorithm²⁶. All atoms interact through potentials calculated from the embedded atom method (EAM)²⁷ and move according to Langevin's equation but with a friction coefficient that decreases as the bond order of the metal atoms increases to mimic the interaction between the NP atoms and the implicit solvent (see figure S1 in supplementary information). The EAM is a local environment-dependent interatomic potential, which is particularly effective in describing metallic systems. For a pure element a , the EAM potential is composed of three functions: the pair energy Φ , the electron density ρ , and the embedding energy F . For an alloy, the EAM potential contains not only the three functions for each of the constituent elements, but also the pair energy Φ_{ab} between different elements a and b . In our code, the potentials are normalized and unified cutoff functions are used, so this energy can be constructed from elemental EAM potentials, as:

$$\Phi_{ab} = \frac{1}{2} \left(\frac{f_b(r)}{f_a(r)} \Phi_{aa} + \frac{f_a(r)}{f_b(r)} \Phi_{bb} \right)$$

where $f_j(r)$ is the electron density at the site of atom arising from atom j at a distance r and Φ_{ij} represents a two body interaction between atoms i and j separated by r . More details can be found in Appendix A of reference 27). The most common way of devising the embedding function and pair potentials is to fit some physically reasonable functional forms to materials properties such as lattice constant and cohesive energies. The potentials used in this work are well fitted to basic material properties such as lattice constants, elastic constants, bulk moduli, vacancy formation energies, and sublimation energies, and they predict reasonably well the heats of solution.

Grand canonical MC simulations were performed in order to compare if some concerted process can affect the growth sequence. The Metropolis Monte Carlo (MMC) algorithm¹¹ was used to sample the configuration space. The importance sample scheme in our gcMC procedure, involves the following trial moves:

Atomic vibration: this is attempted within a small region, around the coordinate of the i atom, and the new configuration is accepted with the probability:

$$W_{j \rightarrow i} = \min \left[1, \exp(-\beta \Delta E_{ij}) \right]$$

Where ΔE_{ij} is the potential energy change associated with the motion of an atom calculated with the embedded atom potential. This trial moves, mimic the lattice vibration as well self-diffusion processes.

Addition of an atom: an attempt is made to insert a Pd atom at a random position on the surface of the NP. The new configuration is accepted with a probability:

$$W_{N_M \rightarrow N_M+1} = \min \left[1, \Gamma \exp \left(\beta \left\{ \mu - \Delta E_{N_M+1, N_M} \right\} \right) \right]$$

where $\Gamma = V_{acc} / \Lambda^3 (N_M + 1)$ and V_{acc} is an accessible volume where the particles are created, Λ is the De Broglie wavelength and $\Delta E_{N_M+1, N_M}$ the potential energy change due to the creation of an atom on the system.

Removal of an atom: a Pd atom is chosen at random and a removal attempt is accepted with probability:

$$W_{N_M \rightarrow N_M-1} = \min \left[1, \Gamma \exp \left(-\beta \left\{ \mu + \Delta E_{N_M-1, N_M} \right\} \right) \right]$$

where $\Gamma = \Lambda^3 N_M / V_{acc}$, $\Delta E_{N_M-1, N_M}$ is the potential energy change due to the elimination of an atom on the system. This trial moves mimic the dissolution process or even more, the equilibrium between species.

4. Results and Discussions

Figure 1 shows the UV-vis spectra of the Au NPs (seeds) before and after the addition of Pd(II) bath. The seeds spectrum (black line) exhibits the characteristic surface plasmon resonance band (SPR) around 510-520 nm, as it is expected for *ca.* 5 nm diameter Au NPs²⁸. Upon the addition of Pd(II) bath, the resulting spectrum only exhibits a gradual increase in absorption toward the blue and a decreasing profile with a noticeably increased

extinction, where the former seeds SPR is barely noticeable near 520 nm. From this evidence, it may be inferred that a Pd shell has been formed and dominates the optical properties of the nanoparticles²⁹. Such a result also suggests the nucleation of Pd NPs is negligible; otherwise the resulting spectrum would retain the Au NPs SPR peak among its main features. This constitutes an indirect corroboration that experimental conditions do contribute to the inhibition of Pd NPs nucleation. However, this observation cannot help in distinguishing whether the attenuation of the Au resonance comes from either the formation of a Pd shell or an Au-Pd surface alloy, since as both scenarios would have similar effects³⁰.

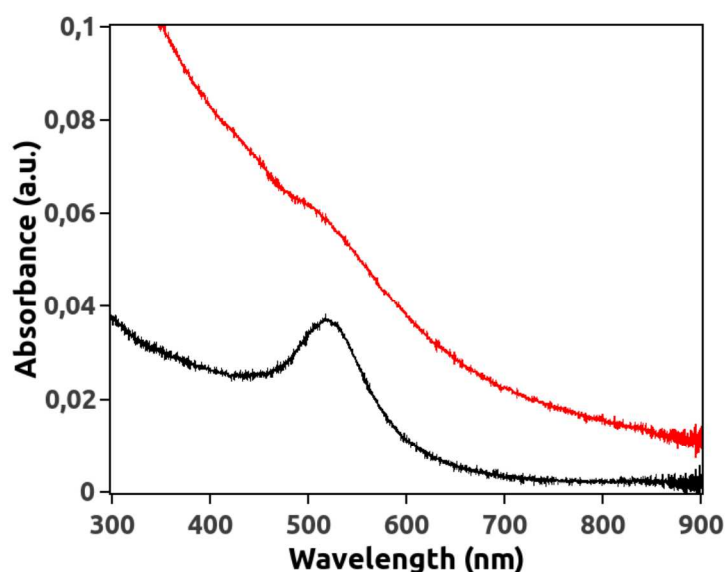


Figure 1: UV-vis spectra of Au seed before (black line) and after (red line) the addition of Pd(II) bath.

The changes in the optical properties as a function of shell thickness have already been predicted. Hofmeister et al.³¹ obtained the theoretical extinction spectra of Au@Pd core-shell nanoparticles with different sizes, based on the Mie-like model. Also, Park and co-workers modeled the extinction spectra of Au@Pd core-shell nanoparticles by using the discrete dipole approximation (DDA) method³². A qualitative agreement between experiment and theoretical trends has been observed for Au@Pd core-shell NPs.

The Au NPs seeds were analyzed using high resolution electron microscopy prior addition of the Pd metastable bath. In figure 2, several TEM and STEM images are shown at different levels of magnification. At low magnification, it can be observed the uniform size distribution of the Au seeds (6 ± 1 nm), whereas at high magnification, a detailed inspection of single seeds does reveal high-index planes on the surface of the NPs (see figure 2c).

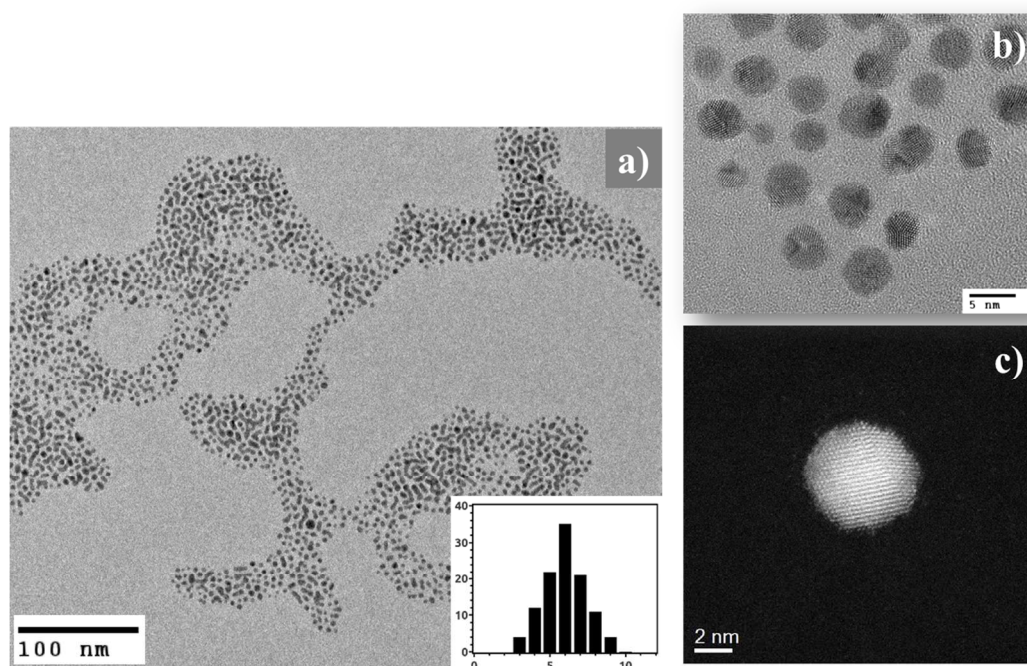


Figure 2: a) Low magnification TEM image of Au NPs seeds (inset: size distribution histogram), b) high-magnification TEM image c) high resolution STEM image taken at 80 kV.

Figure 3(a) displays a representative HAADF-STEM image of the sample, five minutes after the last addition of Pd(II) bath, confirming the presence of Au@Pd core-shell nanoparticles. The STEM image shows a clear contrast difference between the core's gold atoms and palladium atoms at the shell due to their different atomic density values. Since the intensity signal depends strongly on the atomic number (Z), the Pd shell appears less intense than the Au core. The calculated diameter of the core of the Au@Pd particles is 6.7

± 0.1 nm, giving an average shell thickness of 1.3 ± 0.8 nm. This value is consistent with the calculated shell thickness (1.39 nm) using the following equation³³:

$$D_{core-shell} = D_{core} \left(1 + \frac{V_{Pd} [Pd]}{V_{Au} [Au]} \right)^{1/3}$$

Where D_{core} is the diameter of the experimentally measured Au core (6 nm), and V_{Pd} and V_{Au} and $[Pd]$ and $[Au]$ are the molar volumes and concentrations of Pd and Au, respectively.

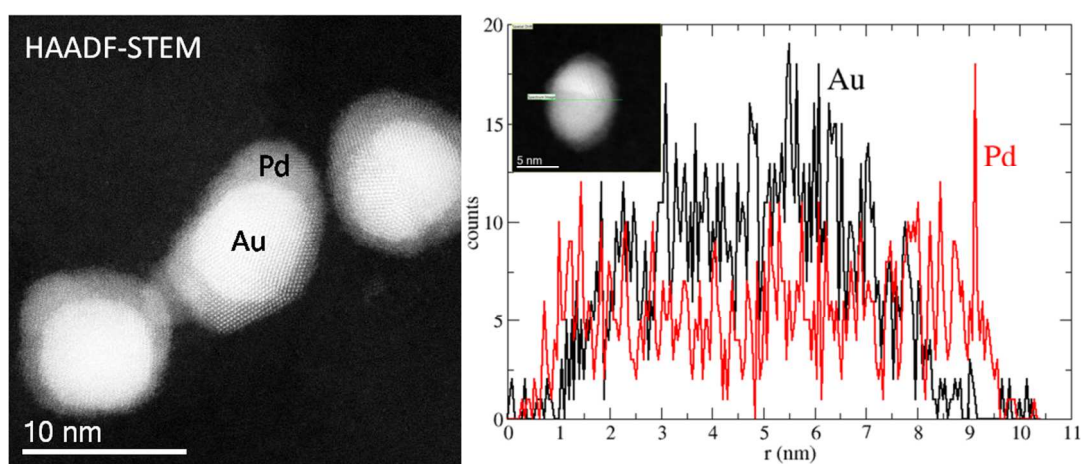


Figure 3: a) HAADF-STEM image of Au(core)-Pd(shell) nanoalloys. b) EDS profile line of a selected nanoparticle.

The distribution of Au and Pd was studied by energy dispersive X-ray spectroscopy (EDS). Figure 3(b) shows the EDS line profile of Au and Pd, measured through the center of an individual nanoparticle (marked by a green line in Figure 3(b)). Both the Au and the Pd signals were clearly traced across the entire particle, but the EDS spectrum indicates that the surface region is enriched with Pd atoms while the core is mainly constituted by Au. It can be noted also how the spheroidal shape of the core seeds is captured by the EDS line profile, in which a higher intensity signal is obtained at the center of the NPs.

It can be stated at this point that the present synthesis route allows to obtain multilayer Au(core)Pd(shell) nanoalloys in all cases. However, as described above, most of

the theoretical calculations predicts Pd(core)Au(shell) structures when consider only 1 ML. Nevertheless, there is a very recent report³⁴ where the effect of multilayers was analyzed. In that work the authors suggest that for large size and multiple ML, the Au(core)Pd(shell) structures could be energetically more stable than Pd(core)Au(shell) ones.

In order to consider different scenarios, the energetic stability of several core-shell structures has been computed using embedded atom potentials and was analyzed by means of the excess energy (Δ) parameter defined as:

$$\Delta = \frac{E_{\text{NP}} - n_{\text{Pd}} E_{\text{Pd}}^{\text{bulk}} - n_{\text{Au}} E_{\text{Au}}^{\text{bulk}}}{(n_{\text{Pd}} + n_{\text{Au}})^{2/3}}$$

where E_{NP} is the total energy of the core-shell NP, $E_{\text{Pd}}^{\text{bulk}}$, $E_{\text{Au}}^{\text{bulk}}$ are the cohesive energy of Pd and Au, respectively and n_{Pd} , n_{Au} de number of Pd and Au atoms in the NP. The more stable a morphological configuration becomes the lower value of Δ parameter³⁵.

Several calculations were performed using different NPs shapes: i.e. single crystal *fcc*-cuboctahedra (CO), and multiple-twinning icosahedra (Ih) and Marks decahedra (Dh). Also the core size and shell thickness were varied in order to analyze variation of stability. In figure 4, excess energy (Δ) as a function of NP diameter is shown for NPs protected by different numbers of shells or monolayers (ML). In the case of NPs covered by only one ML the Au@Pd system is more stable for NPs with size smaller than 2 nm in diameter, whereas for larger sizes, Pd@Au core-shell structures are thermodynamically preferred. Interestingly, as the number of shells protecting the core increase, the crossover occurs at larger sizes. For instance, for two ML it appears at sizes near 4.5 nm in diameter and for three ML it is expected at c.a. 6.5 nm by interpolation.

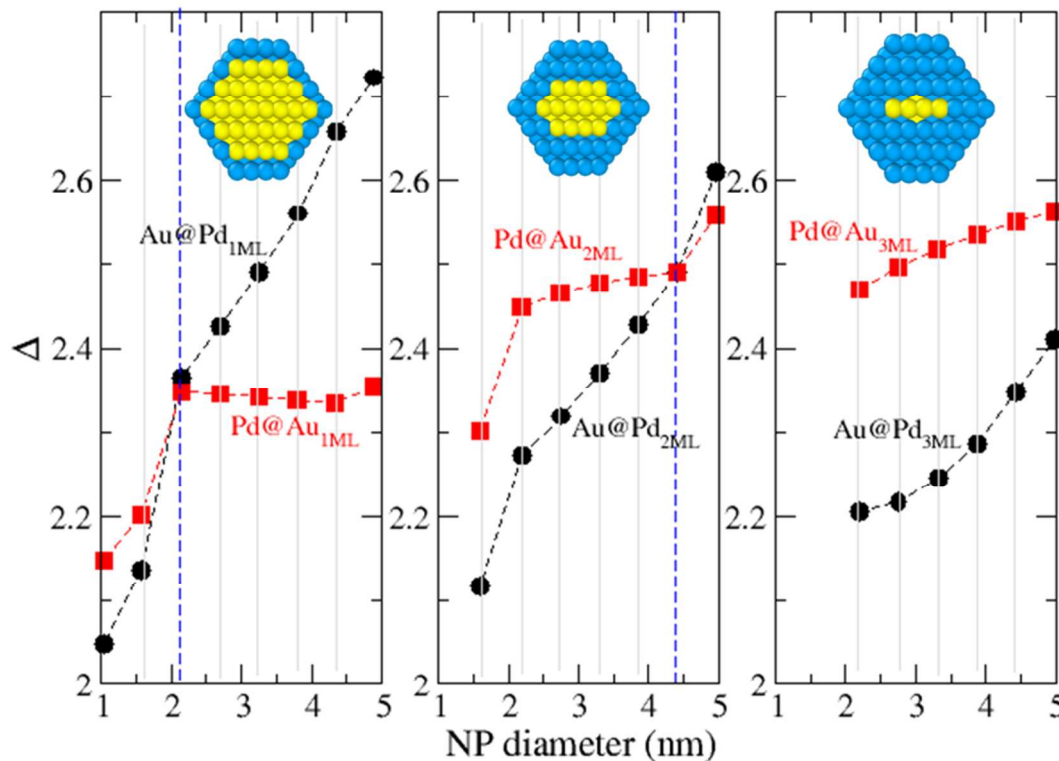


Figure 4: Excess energy as a function of NP size for core-shell with different shell-thickness (1 ML, 2 ML and 3 ML) for the case of CO geometry.

This curious behavior has been observed for all nanoparticle shapes and is shown in figure S3 and S4 in supplementary information.

Full atomistic simulations using two different sampling algorithms were performed with the aim of understanding the growth mechanism of Au@Pd core-shell NPs with different core shapes. In this sense, we have chosen (Dh) and truncated octahedral (*fcc*-TO) geometries due that both NPs morphologies are commonly observed in experimental STEM micrographs.

In figure 5, selected snapshots taken during different simulation stages are shown for (Dh) gold cores. In frames (a-c) the results of gcMC are presented, whereas in frames (d-f) the gcLD ones are shown. As observed by inspection of the atomic configurations, at early stages of the deposition process, Pd atoms starts to nucleate on the (111) faces, close to the edges, a phenomenon observed using both sampling algorithms.

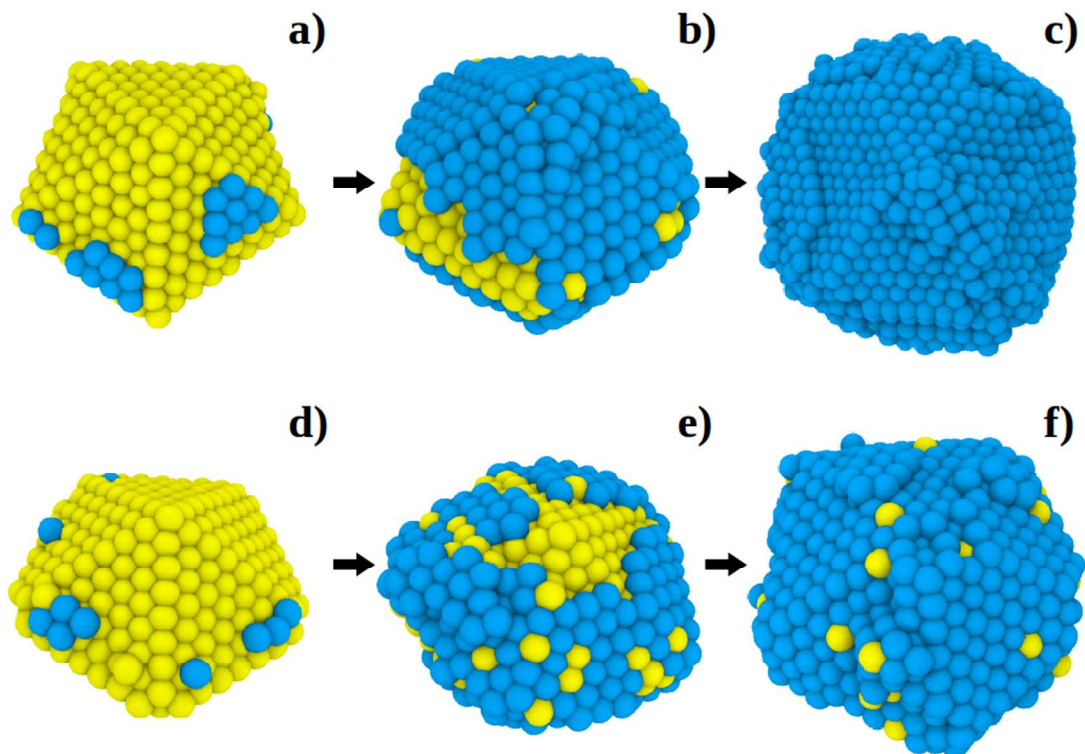


Figure 5: Snapshots taken during evolution of Pd (blue) deposition on the Au (yellow) decahedron at $T = 300$ K, $\mu = 1$ eV: gCMC (upper panel) and gLD (lower panel). Solution atoms are not shown for simplicity. a and d: $\text{Au}_{95}\text{Pd}_5$. b and e: $\text{Au}_{65}\text{Pd}_{35}$. c: $\text{Au}_{15}\text{Pd}_{85}$. f: $\text{Au}_{45}\text{Pd}_{55}$.

As the number of Pd atoms increases, the second Pd layer starts to grow before the first ML is completed, i.e. a layer-by-layer growth mechanism is never observed. However it should be noted that the gLD sampling algorithm shows some degree of surface alloys, even at intermediate stage, i.e. before the gold seed is completely covered by palladium. The nature of the intrinsic dynamics, which is capable of reproducing concerted diffusion mechanisms, may possibly be responsible for the observed discrepancy between Metropolis Monte Carlo and Langevin dynamics results.

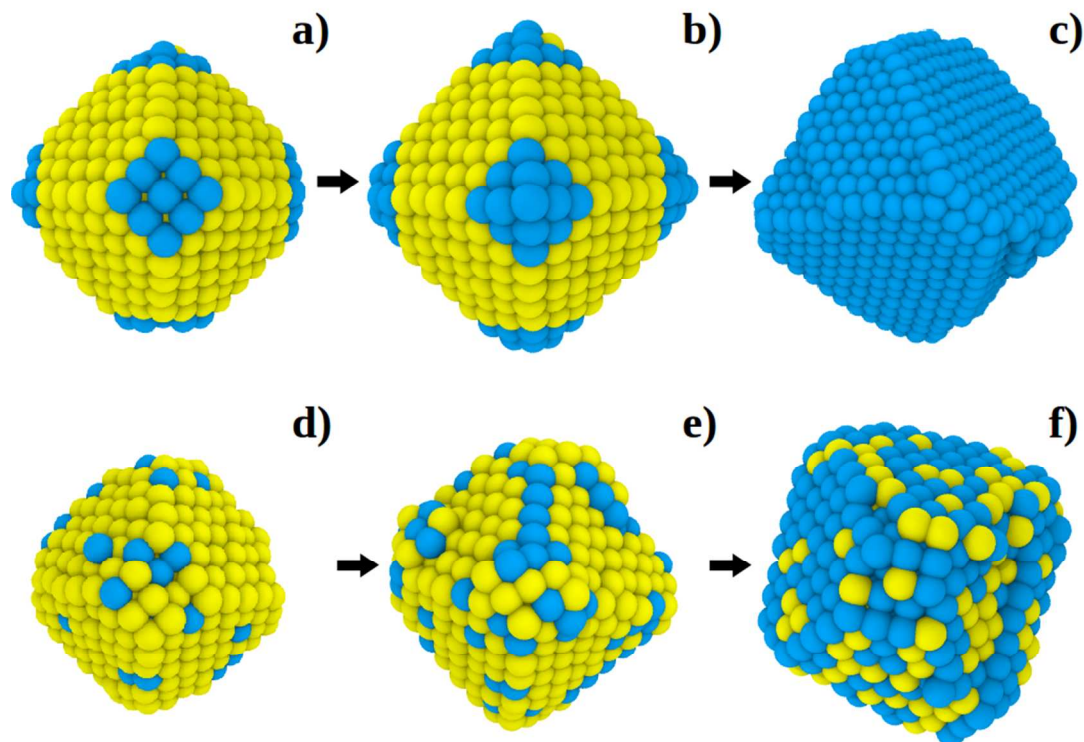


Figure 6: Snapshots taken during evolution of Pd (blue) deposition on the Au (yellow) truncated octahedron at $T = 300$ K, $\mu = 1$ eV: gcMC (upper panel) and gcLD (lower panel). Solution atoms are not shown for simplicity. a and d: $\text{Au}_{95}\text{Pd}_5$. b and e: $\text{Au}_{85}\text{Pd}_{15}$. c: $\text{Au}_{30}\text{Pd}_{70}$. f: $\text{Au}_{60}\text{Pd}_{40}$.

As mentioned above, the same kinds of simulations were performed for other core shapes. For instance, in figure 6 the gcMC and gcLD results for Pd growth on gold cores with truncated octahedral shape are shown. In this case the results are somewhat different. At early stages of Pd atoms deposition, the (100) facets seem to be preferred in both simulation techniques. However, in the case of gcLD, some degree of mixing between Au and Pd is evident, in agreement with the results presented before for Dh structures. Again, the second Pd layer starts to grow before the first Pd ML is completed. The final structures obtained with both methods are different in this case, whereas in the case of gcMC a core-shell structure is observed, the gcLD shows a core-shell structure with mixing of elements at the surface (see a cross-section of this structure in figure S5 – supplementary information). The later structure, has been observed experimentally by many other authors^{13,36}. It can be summarized at this point, that the atomistic simulations are an important tool to predict structures, which can be directly correlated with those observed in

the experiments (see an EDS profile comparison between simulation and experiment in figure S10 – supplementary information). But, it cannot be forgotten that in conventional experiments, NPs are not likely to be restricted to vacuum. Conversely, NPs are generally exposed to solvents, and this causes friction. In such cases sporadic high velocity collisions will perturb the system, and can generate different structures and evolutionary phenomena. In this sense the gcLD results should be more realistic than molecular dynamics or Monte Carlo simulations.

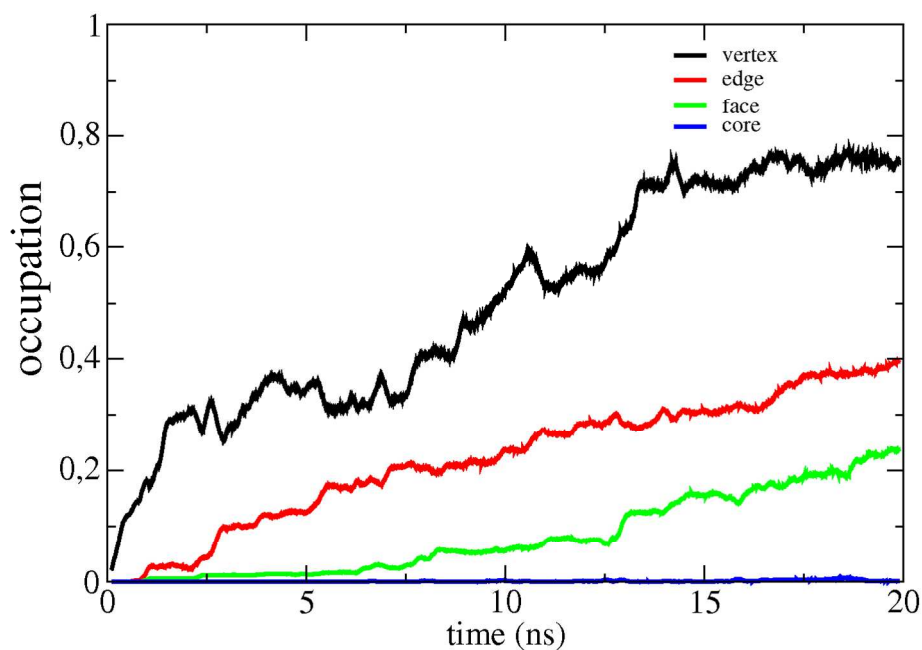


Figure 7: Relative Pd occupation of each site of the decahedron.

With the purpose of quantify in more detail how the deposition of Pd atoms proceed through different atomic sites, we computed the occupation number as a function of time. The different sites are determined by the coordination number of each atom. The internal atoms are bonded to 10 or more atoms. Coordination between 9 and 6 correspond to facets, while coordination of 5 and 4 are matched to edge sites. Lower coordination numbers are consistent with vertex atoms. In figure 7, the relative occupation of each site (i.e. vertex, edges, facets and internal-core) are plotted against simulation time for the case of Dh gold seeds. As observed, the vertex atoms are initially occupied, followed by edges and facets. In the case of TO gold seeds (figure 8), vertex and edges sites are occupied firstly and facets and internal core sites subsequently. This information gives a clear picture on how

the growth mechanism evolves towards the final core-shell structures observed experimentally.

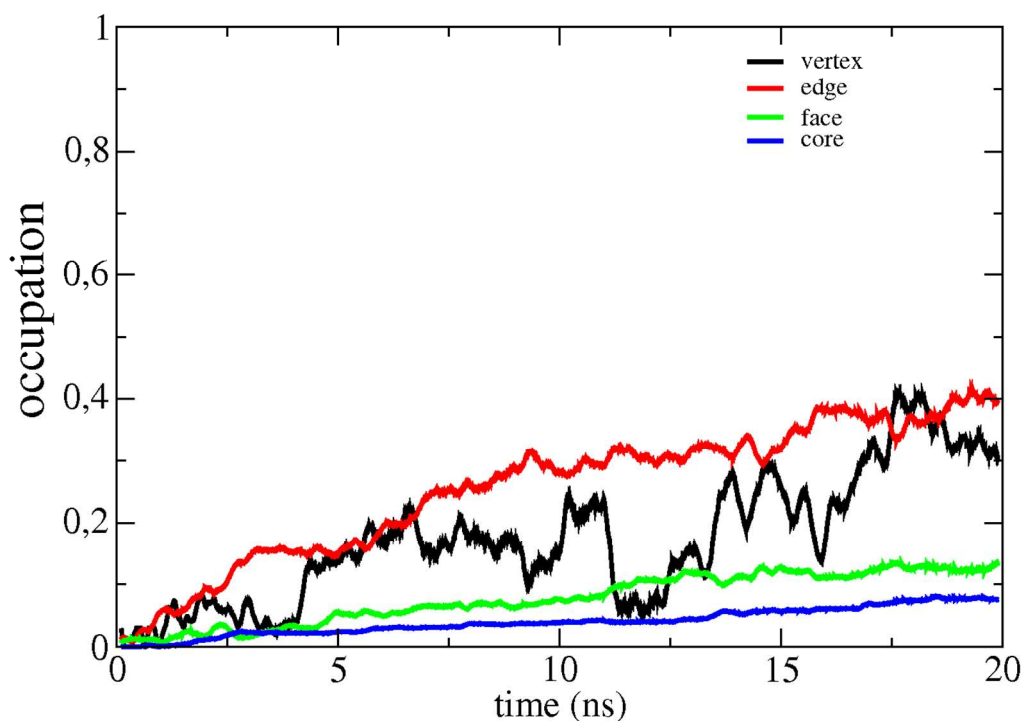


Figure 8: Relative Pd occupation of each site of the truncated octahedron.

The atomic configurations showed in Figures 5c, 6c, 5f and 6f (obtained with gcMC and gcLD respectively) were used as input to simulate HAADF-STEM images. For these simulations we used the multislice method as implemented in the *xHREM* package³⁷, by Ishizuka³⁸ that uses an algorithm based on Fast Fourier Transforms. In the simulated HAADF-STEM, the particle acting as a sample was dissected into 20 slices (in the direction of the electron beam), each slice treated independently through an averaged projected potential. In accordance with the experimental STEM images used in this study, the simulated microscope was set at an electron beam voltage of 200 kV, with a resolution close to 0.1 nm. The simulated micrographs and the experimental STEM images are presented in Figure 9. Remarkably, all the simulated micrographs resemble those obtained experimentally and a direct comparison between experimental images with atomistic simulation results can be done. In both cases, the regions enriched in Au appear brighter than the regions rich in Pd, since the intensity signal depends strongly on the atomic number (Z). The core-shell structure is clearly visible in the structures of the upper panel,

while in the bottom one the mixing of the two species in the surface is more noticeable. It is important to highlight how the simulations qualitatively reproduce the experimental results, providing, at the same time, valuable insight into the growth mechanism. In addition, the supporting information Figure S6, S7, S8 and S9 shows the structure were rotated 0° , 45° and 90° on y- and x-axes.

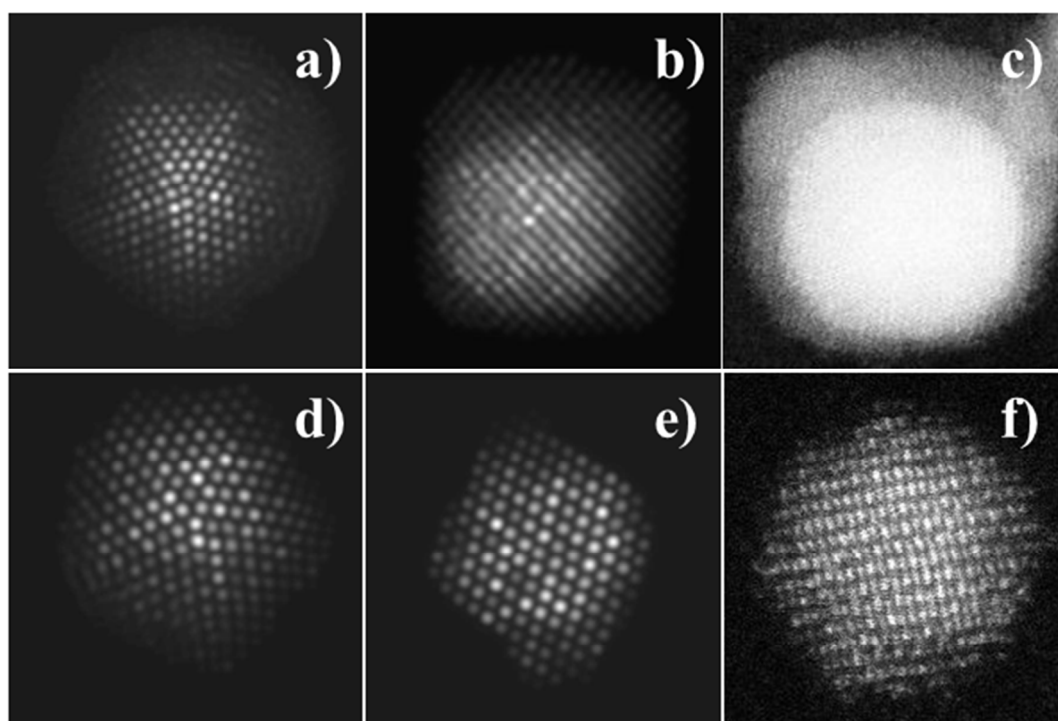


Figure 9: Simulated HAADF-STEM images of Au(core)-Pd(shell) bimetallic nanoparticles. a) and b) Dh structure taken from gcMC and gcLD simulations respectively; d) and e) *fcc*-TO structure taken from gcMC and gcLD simulations respectively. c) and f) are experimental STEM images of the sample.

Conclusions

In summary, gold-palladium core-shell nanoalloys have been produced through a facile synthesis method, where pre-synthesized gold seed were covered by few Pd monolayers. It should be stressed that the synthesis route does not use any surfactant or protective organic molecule to prevent coalescence. Aberration corrected HAADF-STEM,

in combination with high resolution spectral and chemical analysis, has allowed us to study the atomic structure of Au@Pd nanoalloys in atomic detail.

Using embedded atom calculations, we were able to establish how the chemical order of core-shell structure of Au@Pd and Pd@Au could be leading to stable configurations, and how the number of Pd or Au ML could affect that stability. In general terms, a crossover between these kinds of core-shell structures depends on the nanoparticle size.

By using gcMC and gcLD, we have been capable to study the nucleation and growth mechanism of Pd atoms on Au seeds with different shapes. The morphologies obtained with these simulations resemble very well with those obtained experimentally.

Acknowledgments

This work was supported by CONICET PIP 11220110100992, Universidad Nacional de Córdoba, ANPCyT Program BID (PICT 2010-1233) for financial support. The authors acknowledge the Texas Advanced Computing Center (TACC) and the Sistema Nacional de Computación de Alto Desempeño (SNCAD). The group of UTSA wish to thanks the National Center for Research Resources (5 G12RR013646-12) and the National Institute on Minority Health and Health Disparities (G12MD007591) from the National Institutes of Health The authors would like to acknowledge to the NSF for support with grants DMR-1103730, “Alloys at the Nanoscale: The Case of Nanoparticles Second Phase and PREM: NSF PREM Grant # DMR 0934218; “Oxide and Metal Nanoparticles- The Interface Between Life Sciences and Physical Sciences”. In addition, the authors would like to acknowledge the support of the Welch Foundation (grant No. AX-1615, “Controlling the Shape and Particles Using Wet Chemistry Methods: The Case of Bimetallic Nanoparticles”.

References:

-
- 1 R. Wang, O. Dmitrieva, M. Farle, G. Dumpich, M. Acet, S. Mejia-Rosales, E. Perez-Tijerina, M. J. Yacaman and C. Kisielowski, *J. Phys. Chem. C* 2009, **113**, 4395–4400.
 - 2 H. L. Liu, C. H. Sonn, J. H. Wu, K.-M. Lee and Y. K. Kim, *Biomaterials* 2008, **29**, 4003.
 - 3 R. Ferrando, J. Jellinek, and R. L. Johnston, *Chem. Rev.* 2008, **108**, 845.
 - 4 H. Zhang, T. Watanabe, M. Okumura, M. Haruta and N. Toshima, *Nature Materials* 2012, **11**, 49–52.
 - 5 J. Xu, T. White, P. Li, C. He, J. Yu, W. Yuan and Y.-F. Han, *J. Am. Chem. Soc.* 2010, **132**, 10398.
 - 6 E. Gross, I. Popov and M. Asscher, *J. Phys. Chem. C* 2009, **113**, 18341.
 - 7 N. El Kolli, L. Delannoy and C. Louis, *J of Catalysis* 2013, **297**, 79-92.
 - 8 L. Zhang, A. Wang, J. T. Miller, X. Liu, X. Yang, W. Wang, L. Li, Y. Huang, Chung-Y. Mou, and T. Zhang, *ACS Catalysis* 2014, **4** (5), 1546-1553.
 - 9 R. W. J. Scott, O. M. Wilson, S. K. Oh, E. A. Kenik and R. M. Crooks, *J. Am. Chem. Soc.* 2004, **126**, 15583-15591.
 - 10 M. S. Chen, D. Kumar, C. W. Yi and D. W. Goodman, *Science* 2005, **310**, 291-293.
 - 11 D. I. Enache, J. K. Edwards, P. Landon, B. Solsona-Espriu, A. F. Carley, A. A. Herzing, M. Watanabe, C. J. Kiely, D. W. Knight and G. J. Hutchings, *Science* 2006, **311**, 362-365.
 - 12 A. Gopalan, D. Ragupathy, H.-T. Kim, K. M. Manesh and K.-P. Lee, *Spectrochimica Acta Part A: Molecular and Biomolecular Spectroscopy* 2009, **74**, 678-684.
 - 13 M. G. Weir, M. R. Knecht, A. I. Frenkel and R. M. Crooks, *Langmuir* 2010, **26** (2), 1137–1146.
 - 14 M. Mariscal, A. Mayoral, J. A. Olmos-Asar, C. Magen, S. Mejía-Rosales, E. Pérez-Tijerina and M. J. Yacamán, *Nanoscale* 2011, **3**, 5013.
 - 15 A. J. Logsdai and R. L. Johnston, *RSC Advances* 2012, **2**, 5863–5869
 - 16 Y. W. Lee, M. Kim, Y. Kim, S. W. Kang, J.-H. Lee and S. W. Han, *J. Phys. Chem. C* 2010, **114**, 7689–7693.
 - 17 D. Ferrer, A. Torres-Castro, X. Gao, S. Sepúlveda-Guzmán, U. Ortiz-Méndez and M. J. Yacamán, *Nano Letters* 2007, **7**, 1701-1705.
 - 18 Li, C., Cai, W., Kan, C. and Fu, G. *Scr. Mater.* 2004, **50**, 1481.
 - 19 Nutt, M. O., Hughes, J. B. and Wong, M. S. *Environ. Sci. Technol.* 2005, **39**, 1346.
 - 20 R. Ismail and R. L. Johnston, *Phys. Chem. Chem. Phys.* 2010, **12**, 8607–8619.
 - 21 F. Pittaway, L. O. Paz-Borbón, R. L. Johnston, H. Arslan, R. Ferrando, C. Mottet, G. Barcaro and A. Fortunelli, *J. Phys. Chem. C* 2009, **113**, 9141.

-
- 22 I. V. Yudanov and K. M. Neyman, *Phys. Chem. Chem. Phys.* 2010, **12**, 5094–5100.
- 23 O.A. Oviedo, L. Reinaudi, M.M. Mariscal and E.P.M. Leiva, *Electrochimica Acta* 2012, **76**, 424–429.
- 24 M. Mariscal, E.P.M. Leiva, K. Pötting and W. Schmickler, *Applied Physics A* 2007, **87**, 385–389.
- 25 W. Schmickler, K. Pötting, and M. Mariscal, *Chem. Phys.* 2006, **320**, 149–154.
- 26 Allen, P. and D.J. Tildesley, *Computer Simulation of Liquids*. 1987: Clarendon.
- 27 Zhou, X., R. Johnson and H. Wadley, *Phys. Rev. B* 2004, **69**, 144113.
- 28 T. Shimizu, T. Teranishi, S. Hasegawa, M. Miyake. *J. Phys. Chem. B* 2003, **107**, 2719–2724
- 29 A. Henglein, *J. Phys. Chem. B* 2000, **104**, 6683.
- 30 M. B. Cortie and A. M. McDonagh, *Chem. Rev.* 2011, **111**, 3713–3735.
- 31 C. Kan, W. Cai, C. Li, L. Zhang and H. Hofmeister, *J. Phys. D: Appl. Phys.* 2003, **36**, 1609–1614.
- 32 D. You Kim, K. Woo Choi, X.-Lan Zhong, Z.-Yuan Li, S. Hyuk Imand and O Ok Park, *CrystEngComm* 2013, **15**, 3385.
- 33 J. H. Hodak, A. Henglein, M. Giersig and G. V. Hartland, *J. Phys. Chem. B* 2000, **104**, 11708–11718.
- 34 A. J. Logsdail and R. L. Johnston, *RSC Advances*, 2012, **2**, 5863–5869
- 35 F. Baletto, Chapter 8 in *Metal Clusters and Nanoalloys. Nanostructure Science and Technology Series*, Springer. Edited by M. M. Mariscal, *et. al* (2013) 243–273.
- 36 S. W. T. Price, J. M. Rhodes, L. Calvillo and A. E. Russell, *J Phys. Chem. C* 2013, **117**, 24858–24865.
- 37 <http://www.hremresearch.com/>
- 38 K. Ishizuka. *Proc. International Symposium on Hybrid Analyses* 1998, 69–72.